INSTITUTE OF PHYSICS PUBLISHING NANOTECHNOLOGY
Nanotechnology **17** (2006) 4367–4373 doi:10.1088/0957-4484/17/17/013

Remanent magnetic states and interactions in nano-pillars

T J Bromwich[1], T Kasama[2,3], R K K Chong[3], R E Dunin-Borkowski[2,3], A K Petford-Long[4,7], O G Heinonen[5] and C A Ross[6]

[1] Department of Materials, University of Oxford, Parks Road, Oxford OX1 3PH, UK
[2] Frontier Research System, The Institute of Physical and Chemical Research, Hatoyama, Saitama 350-0395, Japan
[3] Department of Materials Science and Metallurgy, University of Cambridge, Pembroke Street, Cambridge CB2 3QZ, UK
[4] Materials Science Division, Chicago National Laboratory, Chicago, IL 60439, USA
[5] Seagate Technology, 7801 Computer Avenue South, Bloomington, MN 55435, USA
[6] Department of Materials Science and Engineering, Massachusetts Institute of Technology, Cambridge, MA 02139, USA

E-mail: petford.long@anl.gov

Received 18 May 2006, in final form 11 July 2006
Published 11 August 2006
Online at stacks.iop.org/Nano/17/4367

Abstract
The remanent magnetic states of rows of electrodeposited nanoscale Ni pillars with diameters of 57–120 nm and aspect ratios of up to 2 have been characterized using off-axis electron holography, which measures the magnetic induction within the pillars and the stray field surrounding them. Inhomogeneities in the Ni, resulting from its grain structure, significantly perturb the axial uniformity of the magnetization. The magnetization is reduced from that of pure Ni due to surface oxidation and the co-deposition of impurities. Interactions between the pillars can be deduced from the external field distribution, and vary with the pillar size and spacing.

1. Introduction

Arrays of magnetic 'nanodots' have been proposed for use in future generations of patterned magnetic recording media [1–3]. Arrays of nominally identical nanodots can be patterned over an area of several cm^2 by various methods, including interference lithography [4, 5]. Such structures provide ideal testbeds for measurements of the magnetic configurations of nanoscale structures and the effects of magnetostatic interactions. High aspect ratio pillars, with an axial magnetization resulting from shape anisotropy, have received considerable attention, and show various remanent magnetic states including 'vortex' and 'flower' states [6–9]. The vortex state is characterized by an in-plane rotation of the moments around the pillar axis, while the flower state is characterized by a near-uniform magnetization. An out-of-plane flower state is magnetized along the pillar axis with a small degree of radial spreading at the top and bottom surfaces, while an in-plane flower state has the magnetization oriented parallel to the flat faces of the cylinder. For pillars with diameters less than a few times the exchange length, an in-plane flower state is stable for aspect ratios $R < R_c = 0.9$ (the aspect ratio, R, is defined as h/b where h is the height of the pillar and b is the diameter), while an out-of-plane (axial) flower state is stable for $R > R_c$ [6, 9, 10]. Vortex or multidomain states are stable in pillars of larger diameter.

In arrays of closely-spaced pillars, measurements and micromagnetic simulations show a reorientation from an out-of-plane to an in-plane easy axis as a function of pillar aspect ratio and spacing, due to magnetostatic interactions [10, 11]. These interactions stabilize particular magnetic configurations, for example in square arrays of axially-magnetized flower-state pillars, 'checkerboard' configurations are stable [6], while strong interactions can reorient the magnetization state observed for a given pillar geometry [11], or the switching fields, e.g. in arrays of low aspect ratio particles [12]. An understanding of these interactions and their effect on the magnetic properties of the array is important for any future

[7] Author to whom any correspondence should be addressed.

 © 2006 IOP Publishing Ltd Printed in the UK

application of magnetic nano-pillars, such as patterned media for high density recording.

Magnetization states and reversal mechanisms in nanoscale materials can be investigated using a variety of techniques, including magnetic force microscopy (MFM) [13], Lorentz transmission electron microscopy (LTEM) [14], off-axis electron holography [15], or by bulk magnetometry measurements, such as alternating gradient magnetometry or superconducting quantum interference device (SQUID) magnetometry [16]. The advantage of electron holography and LTEM is that *in situ* magnetizing experiments can be conducted and phase contrast images of remanent magnetic states can be obtained with very high spatial resolution [17]. However, these techniques are rarely applied to arrays of nanoscale pillars because of their axial magnetization, which requires the pillars to be imaged from the side and is therefore inconvenient for a 2D array. Due to the geometry of the pillars and the large influence of the mean inner potential of the specimen on the contrast, LTEM is not suitable for the analysis of pillars imaged from the side [18].

In the present work, the remanent states of various magnetic pillar samples with diameters of 57–120 nm and aspect ratios of up to 2 have been characterized using off-axis electron holography after applying a magnetic field. The pillars are expected to be magnetized in an out-of-plane flower state, so we prepared 1D rows of pillars, which could be imaged perpendicular to their length. This enabled inhomogeneities in the magnetization along the axis of the pillars, and the interactions between the pillars, to be analysed.

2. Experimental details

Large area arrays (several square centimetres) of Ni pillars were fabricated using interference lithography. In this process, a laser beam is split into two beams which are recombined to form an interference pattern of fringes on a resist-coated substrate. Two sequential exposures were used to form a square array of cylindrical holes in a tri-layer resist stack. The pillars were then fabricated using electrodeposition to fill the holes in the resist stack. The procedure is described in detail elsewhere [6, 19]. The substrate was a silicon wafer coated with a conductive layer of 5 nm of Cr and 5–20 nm of Au. The pillars formed a square array of period 100 or 200 nm, and had diameters ranging from 57 to 120 nm and heights ranging from 115 to 240 nm.

Transmission electron microscopy (TEM) specimens were prepared from the square arrays of pillars using a focused ion beam (FIB) system. These samples were prepared in such a way that a single row of pillars could be imaged in cross-section. In order to protect the pillars from the potentially damaging effects of implantation and physical damage to the specimen, the sample was first coated with a 200–500 nm layer of amorphous carbon. A 1 μm-thick strip of Pt was then deposited onto the carbon layer. A single row of pillars was cut out of the array using a 30 kV Ga^+ ion beam by the lift-out method [20], and placed on a carbon-coated Cu TEM grid in the form of a cross-sectional specimen that was one pillar thick. The presence of the layer of amorphous carbon under the protective Pt strip meant that during the final stage of the milling process the Pt strip fell off the sample without the need for further milling to remove it. There was no measurable contamination of the specimen by Pt or Ga, according to energy-dispersive x-ray analysis in a JEOL 2010 TEM equipped with an Oxford Instruments LZ5 windowless detector. The minimum detectable Ga content is estimated to be of the order of 2 at.%.

Off-axis electron holography was carried out using an incident electron energy of 300 kV in a Philips CM300-ST TEM, equipped with an electron biprism. A detailed description of the technique of off-axis electron holography can be found elsewhere [15]. Holograms of remanent magnetic states were acquired using a Lorentz mini-lens, which allows the specimen to be imaged in a magnetic-field-free environment with the conventional microscope objective lens switched off. The objective lens current can, however, be increased in order to apply a known magnetic field to the specimen parallel to the electron beam direction. In order to record each remanent magnetic state, the specimen was first oriented by tilting to the Si substrate $\langle 110 \rangle$ zone axis. The specimen was then tilted by $+30°$ (see schematics in figures 1(a) and (b)), and the objective lens current was increased in order to use the lens field to saturate the magnetization along the pillar axis (i.e. in the plane of the cross-sectional specimen) in one direction. The objective lens current was then reduced to zero, the sample was tilted to $-30°$, and the objective lens current was increased to provide the desired component of magnetic field in the plane of the specimen along the pillar axis. Finally, the objective lens current was again reduced to zero and the sample tilted back to the $\langle 110 \rangle$ zone axis for acquisition of the holograms. It should be noted that, because the field was applied at 30° to the pillar axis, there was a component of the applied field perpendicular to the pillar axis during the magnetizing process that is twice as large as the component parallel to the pillar axis. This procedure was repeated for different values of the applied field, in order to record a series of holograms corresponding to a remanent hysteresis loop. Reference holograms were recorded from vacuum after each hologram of the specimen in order to remove artefacts associated with the imaging and recording system of the microscope.

The mean inner potential (MIP) contribution to the holographic phase shift was determined by evaluating half of the sum of phase images between which the magnetic state of the specimen had reversed exactly. This MIP contribution to the phase shift was then subtracted from each individual phase image of the specimen, to obtain the magnetic phase shift, the parameter of primary interest. The image processing was all conducted using the Semper software [21]. The remanent magnetization states record only the irreversible parts of the magnetization reversal process, and the specimen is saturated between successive images so the images presented here do not represent a single, continuous hysteresis loop. The applied field spacing between holograms was 30 Oe in the switching region and the maximum applied field was 1500 Oe. In total, up to 13 images were taken in each applied field direction for each specimen.

Electron tomography of a 75 nm diameter 175 nm high Ni sample was carried out using an FEI Tecnai F20-G2 FEGTEM and an ultra high-tilt tomography specimen holder. A series of images was acquired over a large range of sample tilt (here $-62°$ to $+56°$) limited only by the sample

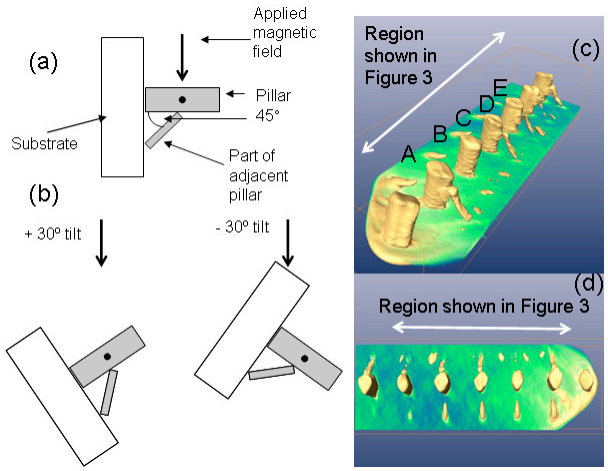

Figure 1. (a) A schematic representation of the geometry of the pillars, including the remaining partial pillar sections and the direction of the magnetic field. (b) The geometry resulting from a rotation of ±30° into the applied field, about the axis indicated by the black dot. (c) and (d) HAADF electron tomography reconstruction of Ni pillars (75 nm diameter, 175 nm height, 200 nm period) on a FIB-milled specimen. The pillars that are shown in the induction maps in figure 3 are indicated and are labelled A–E. The oblique view (c) and plan view (d) image show the presence of 'partial pillars' which result from the incomplete removal of adjacent pillars during sample preparation. In the plan view, pillar A is second from the right and pillar E second from the left.

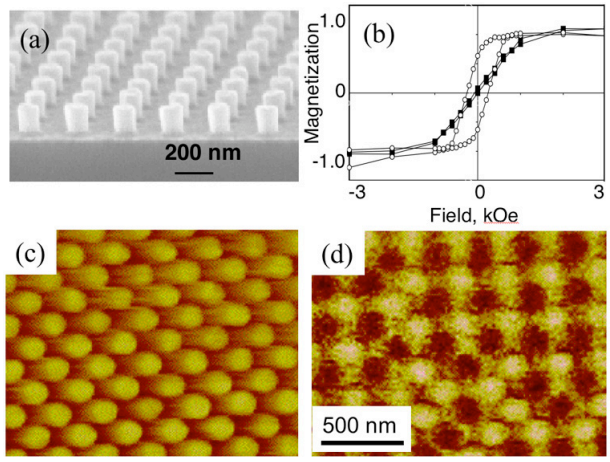

Figure 2. (a) Scanning electron micrograph and (b) normalized hysteresis loop taken using vibrating sample magnetometry of Ni pillars, 125 nm tall, 92 nm diameter, 200 nm period. The open symbols show the out-of-plane loop and the filled symbols the in-plane loop. (c) Topographic AFM image (vertical full scale 200 nm), (d) MFM image (full scale 1.5 degrees of phase) of 220 nm tall, 200 nm period Ni pillars.

geometry, and then mathematically reconstructed to obtain a 3D visualization of the sample [22]. The signal used was the high-angle annular dark-field (HAADF) signal. The contrast in this mode arises from atomic number differences in the specimen. HAADF contrast was used as it minimizes the diffraction contrast contributions to the images. The inner detector angle for the HAADF images used for tomographic reconstruction was approximately 50 mrad. Two views of a tomographic reconstruction of a specimen containing pillars of diameter 75 nm, height 175 nm and period 200 nm, obtained from electron tomography, are shown in figures 1(c) and (d). The electron tomography reconstructions suggest that the cylindrical cross-section of the pillars is preserved by the sample preparation process, but several of the pillars show a buttress-like feature which is a small section of a pillar remaining from the adjacent row, cut by the FIB.

Micromagnetic modelling of the pillars was carried out for comparison with the experimental measurements. The simulations involved solving the Landau–Lifshitz–Gilbert (LLG) equations using a Bulirsch–Stoer adaptable-time-step method [23] parallelized and optimized for the LLG equations. The dimensionless damping constant was set to 0.25 in order to achieve rapid convergence to an equilibrium state. Rows of five or six pillars each 80 nm in diameter and 160 nm in height were modelled. The magnetocrystalline anisotropy of the pillars was set to 12 Oe along the pillar axes, and disorder in this anisotropy was included by using a Gaussian random component with a standard deviation in field of 4 Oe and in angle of 5° between cells. The exchange coupling was 1.2×10^{-6} erg cm^{-1} and the cell size used was 5 nm × 5 nm × 5 nm. Some calculations were repeated with a cell size of 2.5 nm × 2.5 nm × 2.5 nm to verify that the cell size did not affect the results. The period of the pillars and the saturation magnetization were varied between 100 and 200 nm and 300 and 450 emu cm^{-3}, respectively, in order to determine the effect of these parameters on the magnetic behaviour of the pillars at remanence. The magnetic configurations of the row of pillars were compared after saturation parallel to the axis followed by application of reverse fields of either 1000 or 100 Oe.

3. Results and discussion

3.1. Array morphology, microstructure and magnetic properties

A side-view scanning electron micrograph of an array of Ni pillars with diameter 92 nm and height 125 nm is given in figure 2(a), together with its hysteresis loop (figure 2(b)). An atomic force (figure 2(c)) and magnetic force microscope image (figure 2(d)) of a similar but taller (220 nm height) sample after ac demagnetization is also shown. The samples were imaged after removal of the electrodeposition template to reveal the cylindrical morphology of the pillars. As described elsewhere [6, 24] and illustrated by the magnetometry data shown in figure 2(b), pillars with dimensions such as these show an out-of-plane flower state. The out-of-plane easy axis hysteresis loop of the array is sheared due to magnetostatic interactions between the pillars, while the in-plane loop is characteristic of a hard axis. Individual cylinders behave like single-domain particles, appearing dark or light in the MFM image depending on their magnetization direction. The checkerboard pattern in parts of the MFM image, showing pillars with alternating magnetization direction, is characteristic of a square array of dipoles interacting magnetostatically. VSM data on a range of Ni pillar samples gives a value of M_s of 320 emu cm^{-3} for the electrodeposited Ni, 66% that of pure Ni, which is attributed to codeposition of impurities from the sulfamate electrolyte.

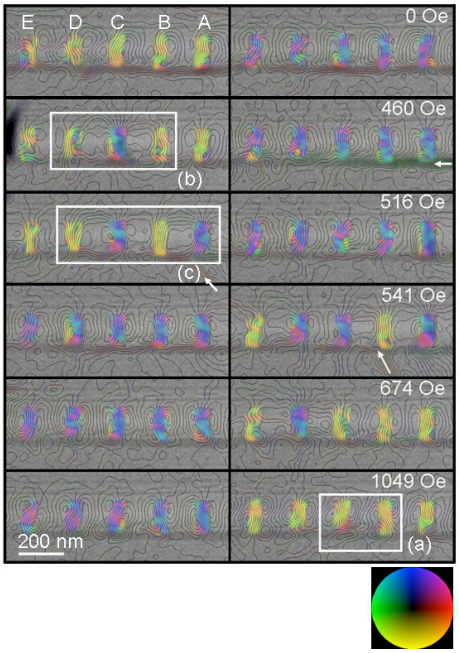

Figure 3. Magnetic induction maps of a single row of Ni pillars that are nominally 75 nm in diameter and 175 nm in height, measured from off-axis electron holography. The colours indicate the direction of the local magnetic induction at remanence, according to the colour wheel shown. The black lines are magnetic phase contours with a spacing of 0.2 rad. The indicated in-plane fields were applied upwards (left column) or downwards (right column), after initially saturating the pillars downwards or upwards respectively. The mean inner potential contribution to the phase shift has been removed from each image (see text for details). Arrows indicate artefacts resulting from the presence of diffraction contrast in the holograms. The labels (a)–(c) indicate particular flux configurations and are explained in the text.

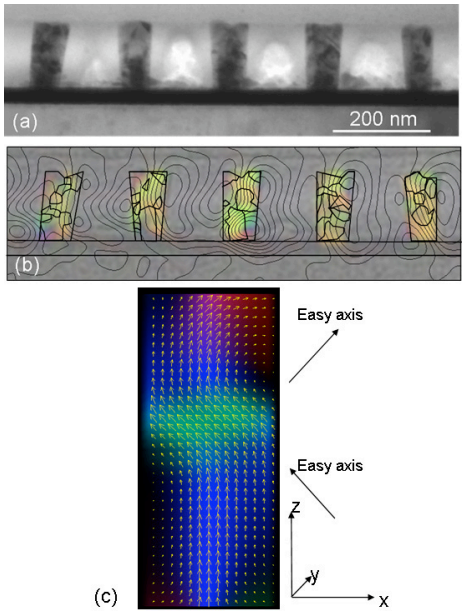

Figure 4. (a) Bright field TEM image of the single row of five magnetic nano-pillars A–E shown in figure 3. (b) A magnetic induction map of the same five pillars with the positions of the grains from the bright field image overlaid. (c) Simulated remanent state of a Ni pillar (75 nm in diameter and 175 nm high) with a grain boundary inserted half way up the pillar long axis. The arrows represent the anisotropy directions in the two halves of the pillar.

3.2. Electron holography

Magnetic induction maps reconstructed from off-axis electron holograms acquired from a single row of pillars from a Ni sample (75 nm diameter and 175 nm high) are shown in figure 3. The local magnetic induction direction in the pillars projected in the incident electron beam direction is indicated by the direction of the phase contours. These contours were generated directly from the magnetic contribution to the holographic phase shift. The magnetic flux enclosed between any two adjacent contours is the same. Colours (visible in the on-line version of the figure) have also been used to highlight changes in the direction of the local magnetic induction, according to the colour wheel shown. The pillars are predominantly single domain at remanence, with their magnetization directions along the pillar axes. However, there are variations in magnetization direction within the pillars, and there is evidence of end domain formation, i.e. of regions at the ends of the pillars where the magnetic moments show a deviation from the axial direction. Bright-field TEM images of this sample show that the grain size in each Ni pillar is approximately 30–40 nm. A correlation between the positions of the grain boundaries and the deviations in the magnetization direction within the pillars was observed, as can be seen in figure 4. The most prominent grain positions have been overlaid onto the magnetic induction map and suggest that the deviations in magnetization direction are related to the different orientations of the crystallographic easy axes with the different grains. Ni has cubic magnetocrystalline anisotropy ($K_1 = -4.5 \times 10^4$ erg cm^{-3}, $K_2 = -2.3 \times 10^4$ erg cm^{-3} at room temperature) with $\langle 111 \rangle$ easy directions. The magnetocrystalline anisotropy is small compared to the shape anisotropy (for example, 2.1×10^5 erg cm^{-3} for a prolate ellipsoid with aspect ratio 175/75 and saturation magnetization 485 emu cm^{-3}), so the shape anisotropy causes the net magnetization to lie along the pillar axis, but with deviations in direction from grain to grain due to magnetocrystalline anisotropy.

The importance of grain boundaries in leading to magnetization deviations has been confirmed by micromagnetic modelling. A simulation was performed for a Ni pillar of the same size and shape as in the sample described above, but containing a grain boundary half-way up the z-axis of the pillar (see figure 4(c)). A magnetocrystalline anisotropy of -4.5×10^4 erg cm^{-3} was included, oriented along two different directions (arrowed) in the top and bottom parts of the pillar. A 90° domain wall was observed at remanence at the position of the artificial grain boundary, associated with local magnetization inhomogeneities.

As mentioned above, figure 3 shows data for both positive and negative applied fields. There is a clear asymmetry in the reversal fields of individual pillars. For example in the left column of figure 3, pillar C reverses magnetically before its neighbours, at a field of less than 460 Oe, as indicated by the colour change in that pillar from yellow to blue. Pillar A is second to reverse, in the field range 460–516 Oe. In

contrast, for the opposite field direction (right column of figure 3), reversal occurs first in pillars B and E in the range 516–541 Oe. (The fields quoted represent the component parallel to the axes of the pillars; the total field is applied at 30° to the pillar axes and higher by a factor of $\sqrt{3}$.) This reversal asymmetry is attributed to the effect of the buttress-like sections of the adjacent row of pillars remaining after the FIB preparation. Pillars B and E show symmetrical reversal while pillars A, C and D do not. The reconstruction obtained from electron tomography (figure 1) indicates that buttress features are present next to these three pillars. Although the magnetic field is applied symmetrically with respect to the axis of the complete pillars, the residual partial pillar sections are angled with respect to the field during the forward and reverse field sweeps. Figures 1(a) and (b) illustrate the sample geometry and the applied field directions. A 30° anticlockwise rotation of the sample prior to field application will result in the partial pillars being aligned almost parallel to the magnetic field of the objective lens, and they will be saturated by the applied field. However, when the sample is instead rotated −30° clockwise, the partial pillars will be saturated in the opposite direction. The applied field H acting on a whole pillar will thus have a component due to the field of the objective lens H_{OBJ} and a magnetostatic component arising from the field of the partial pillar H_{PP}, as follows:

$$\text{Anticlockwise} \qquad H = -H_{\mathrm{OBJ}} \sin 30 \pm H_{\mathrm{PP}} \cos\theta \qquad (1)$$

$$\text{Clockwise} \qquad H = H_{\mathrm{OBJ}} \sin 30 \pm H_{\mathrm{PP}} \cos\theta \qquad (2)$$

where θ is the angle between the partial pillar and the whole pillar axes. The total applied field in the clockwise rotation differs, with respect to the anticlockwise rotation, by a factor of $2H_{\mathrm{PP}} \cos\theta$. θ can be estimated from the tomography data as approximately 45° and the difference in reversal field of the pillars can be taken from the electron holography data as approximately 200 Oe, thus a value for H_{PP} of 141 Oe is obtained. This is a reasonable magnitude for the magnetostatic field from a partial pillar. For example the field 20 nm from the end of a Ni rod, 175 nm long and 20 nm diameter, with $M_{\mathrm{s}} =$ 320 emu cm^{-3}, can be estimated as ∼250 Oe. Previous work has shown that the pillars are coated with a thin layer of oxide due to atmospheric exposure [6], so it is unlikely that there will be strong exchange coupling between the partial pillars and the whole pillars, and the interactions are magnetostatic.

3.3. Interactions between pillars

The checkerboard pattern of magnetization, in which adjacent pillars in a square array have opposite magnetization directions after an ac demagnetization process (figure 2(d)), provides evidence for significant magnetostatic interactions between pillars. The nearest neighbour interaction field (H_{int}) between parallel dipoles is given by

$$H_{\mathrm{int}} = \frac{M_{\mathrm{s}} V}{p^3} \qquad (3)$$

where M_{s} is the saturation magnetization, V is the pillar volume and p is the period. For the sample of figure 3, using a dipolar model and a saturation moment of 320 emu cm^{-3}, the nearest neighbour interaction field would be 31 Oe, compared with the measured switching fields of order 500 Oe.

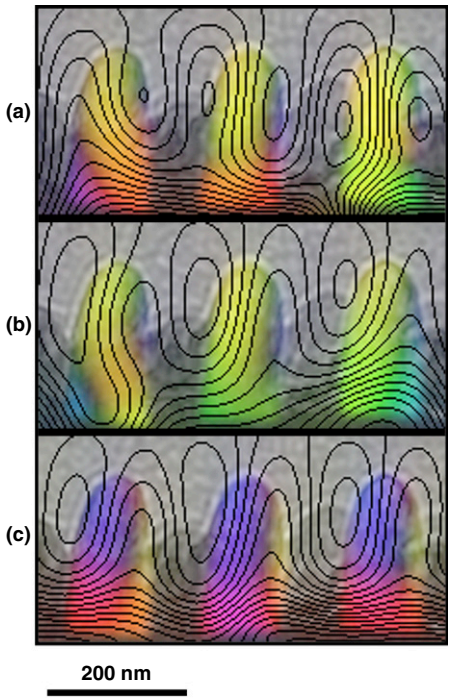

Figure 5. Magnetic induction maps showing a row of NiCo pillars 120 nm in diameter and 240 nm tall, with 200 nm period, at remanence after saturation followed by a reverse field of (a) 0 Oe, (b) 193 Oe, (c) 1050 Oe. The phase contours have a spacing of 0.04 rad.

The phase contours of the induction maps of figure 3 show the stray field patterns between the pillars. The phase contours have a spacing of 0.2 rad. Examples of several different magnetization configurations of neighbouring pillars are indicated in figure 3 by the labels (a)–(c). The two pillars in (a), which have parallel magnetization, show flux lines leaving the top of each pillar and closing at the pillar base, with little flux linkage between the pillars. When neighbouring pillars are oppositely magnetized as seen in (b), a flux closure structure between neighbours is created which stabilizes the magnetic state, as in the antiparallel alignment seen in the checkerboard arrangement of the 2D square array. The example labelled (c) shows four pillars, with alternate pillars oppositely magnetized, and flux closure between pairs of pillars. The stray field distributions imaged in the induction maps provide the contrast mechanism for MFM images such as figure 2(d).

Striking differences in the stray field configuration were observed when either the pillar spacing was reduced or the pillar size was increased for a given pillar spacing. Figure 5 shows NiCo pillars of diameter 130 nm, 240 nm high and 200 nm period. The magnetization is axial at the upper part of the pillars, but lies in plane near the base, and the pillars often contain 90° domain walls. Similar non-uniform magnetization configurations were observed at remanence after applying reverse fields of up to 1050 Oe. The NiCo has a saturation moment of ∼900 emu cm^{-3}, and an exchange length about one third that of the electrodeposited Ni. The NiCo

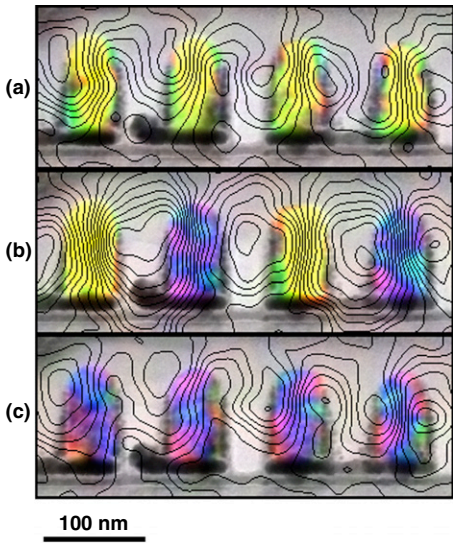

Figure 6. Magnetic induction maps showing a row of Ni pillars 57 nm in diameter and 115 nm tall, with 100 nm period, at remanence after saturation followed by a reverse field of (a) 0 Oe, (b) 450 Oe, (c) 920 Oe. The phase contours have a spacing of 0.049 rad.

pillars are well within the vortex or multidomain region of the magnetic phase diagram [6] leading to the appearance of complex magnetization states.

Figure 6 shows parts of a row of Ni pillars 57 nm in diameter and 115 nm high with period of 100 nm. After saturation, the pillars are mostly magnetized 'down', although one pillar had reversed under the influence of the field from its neighbours. At higher reverse fields, e.g. 450 Oe (b), alternating 'up' and 'down' magnetization directions are seen in small groups of pillars with flux closure between neighbours. After reverse fields of 900 Oe or more (c) the pillars are all magnetized 'up'. In contrast to the larger Ni pillars, and to the NiCo pillars, these pillars show more uniform magnetization states, with no evidence of domain walls or in-plane magnetization.

To interpret these results, micromagnetic modelling of rows of five and six pillars was carried out for different pillar spacings and values of saturation magnetization. Figure 7 shows maps of the magnetization induction field **B** for the central slice through a row of pillars with a diameter of 80 nm and a height of 175 nm at two different centre-centre spacings of (a) 100 nm and (b) 200 nm. In each case the saturation magnetization was 450 emu cm^{-3}. The maps show a vortex configuration at the top and bottom surfaces of the pillar, although there is a significant component of axial magnetization. Flux exits the sides of the pillars, which is characteristic of the vortex state. With small spacing between the pillars (figure 7(a)), there are strong magnetostatic interactions between adjacent pillars, and large amounts of flux exiting the side of one pillar enter the side of a neighbouring pillar. As the spacing is increased to 200 nm (figure 7(b)), the magnetostatic interactions are much reduced, and the flux from each pillar returns largely in the space between the pillars. The effect of changing the saturation magnetization of the pillars is seen in figure 8. The saturation magnetization (M_s) used for the simulations was (a) 400 emu cm^{-3} and (b) 300 emu cm^{-3}.

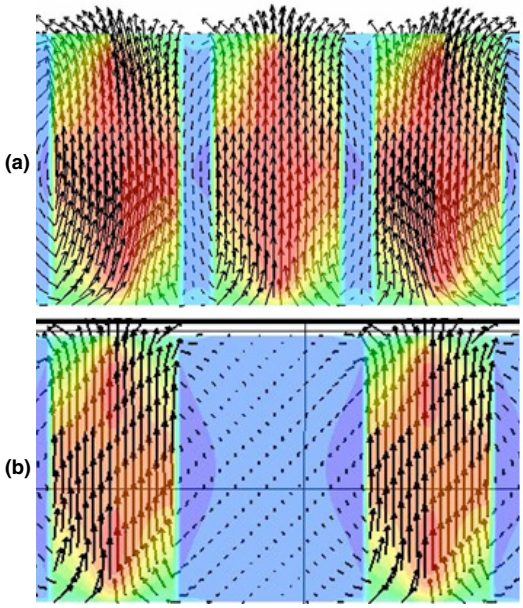

Figure 7. Calculated magnetic induction maps of the central slice through a row of Ni pillars (shaded dark) that are each 80 nm in diameter and 175 nm in height generated using finite element modelling. Arrows show the direction of magnetic flux, and the lengths of the arrows are proportional to the local magnitude of **B**. The period of the pillars was varied from 100 nm in (a) to 200 nm in (b). The value of M_s used was 450 emu cm^{-3}, the exchange coupling was 1.2×10^{-6} erg cm^{-1} and the cell size used was 5 nm $\times$ 5 nm $\times$ 5 nm.

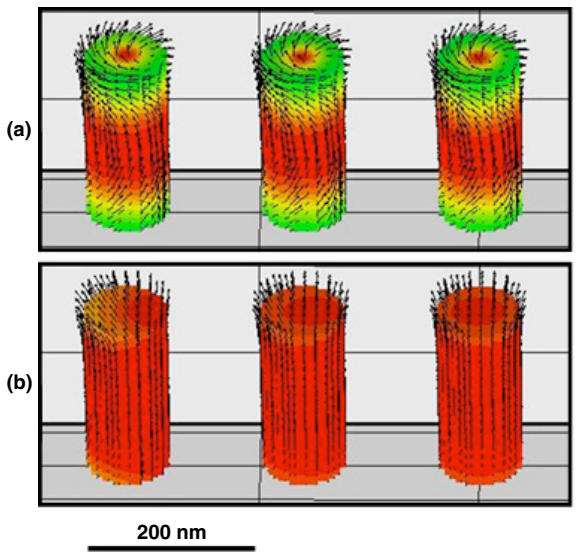

Figure 8. Calculated three-dimensional magnetization density distribution in a single row of Ni pillars, showing the effect of magnetization for pillars that are 80 nm in diameter, 175 nm in height with a 200 nm spacing. (a) $M_s = 400$ emu cm^{-3}, and (b) $M_s = 300$ emu cm^{-3}. The exchange coupling was 1.2×10^{-6} erg cm^{-1} and the cell size used was 5 nm $\times$ 5 nm $\times$ 5 nm.

A lower M_s increases the exchange length and pushes the flower-vortex transition to higher diameters, so the lower moment pillars are in the out-of-plane flower state and the flux

exits the pillar primarily at the top and bottom surfaces. The stray field distribution seen in the reconstructed phase images is more consistent with the micromagnetic configuration seen in figure 7(b), and confirms that the saturation magnetization in the pillars is lower than the bulk value for Ni.

In the absence of applied fields outside the specimen, B_r, the magnetic induction at remanence, can be calculated from the magnetic phase shift (ϕ_m) across the pillar by using the equation:

$$\phi_m = \frac{e}{\hbar c} B_\perp \int_{-\infty}^{x} t \, dx \tag{4}$$

where $B_\perp$ is the magnetic induction in a direction perpendicular to the optical axis of the electron microscope (z), x is the pillar radius and t is the material thickness. Assuming a pillar of infinite length and no stray fields, the change in the magnetic phase shift across a pillar of diameter 75 nm and height 175 nm with $M_s = 320$ emu cm^{-3} is predicted to be 2.15 rad. This is reduced significantly to 1.29 rad when demagnetizing fields (both internal and those resulting from similarly magnetized neighbours) are included using a Fourier space approach based on the work of Beleggia and Zhu [25]. The actual phase change measured from the magnetic induction maps is 1.05 rad, giving a value of M_r of 208 emu cm^{-3}. The value of M_r is still significantly below the value of M_s (320 emu cm^{-3}) measured for the as-plated pillars. This reduction can be accounted for by surface oxidation of the pillars, or by the presence of Ga implantation at a level that is lower than that detectable by EDX. Our previous work [26] showed that Ga implantation at a level of only a few ppm is enough to modify the magnetic properties of a thin NiFe film. An oxide layer of a few nm thickness has been observed previously around Ni pillars and nanoparticles [6, 27]. If the radius of the pillar is reduced by 5 nm, the value of M_r calculated from the experimental data is 320 emu cm^{-3}, which is in agreement with the value measured using VSM, and suggests that the pillars are saturated at remanence.

4. Conclusions

We have analysed a series of magnetic nano-pillar samples in cross-sectional TEM specimens using off-axis electron holography. A series of remanent state holography images showed a significant asymmetry in the reversal field, which could be accounted for by the presence of partial pillars adjacent to the pillars of interest. Ni pillars were generally single domain, but deviations of the magnetization from the axis of polycrystalline pillars were correlated with the presence of microstructural features such as grain boundaries. Pillars of NiCo, which has a smaller exchange length, showed evidence of multidomain or vortex states. Imaging of the stray fields around the pillars showed how the flux closure depended on the magnetic state of neighbouring pillars, while quantitative analysis of the flux confirmed that the 75 nm diameter pillars are saturated at remanence, with a magnetization in agreement with that measured by magnetometry. The unique information gained from electron holography on magnetization states and inter-pillar interactions will be valuable in assessing the suitability of such nanostructures for applications such as high density patterned media.

Acknowledgments

TJB would like to thank the EPSRC and Trinity College, Oxford for funding. CAR acknowledges the support of the National Science Foundation, and thanks M Farhoud, T Savas and W Schwarzacher for sample preparation. Argonne National Laboratory is supported by the US Department of Energy, Basic Energy Sciences–Materials Sciences, under contract no. W-31-109-ENG-38. RDB thanks the Royal Society.

References

[1] Chou S Y 1997 *Proc. IEEE* **85** 652
Chou S Y, Krauss P R and Kong L 1996 *J. Appl. Phys.* **79** 6101
[2] Ross C A 2001 *Ann. Rev. Mater. Res.* **31** 203
[3] White R L, New R M H and Pease R F W 1997 *IEEE Trans. Magn.* **33** 990
[4] Rousseaux F, Decanini D, Cascenac F, Cambril E, Ravet M S, Chappert C, Bardou N, Bartenlian B and Viellet P 1999 *J. Vac. Sci. Technol.* B **17** 3168
[5] Ross C A, Farhoud M, Hwang M, Smith H I, Redjdal M and Humphrey F B 2001 *J. Appl. Phys.* **89** 1310
[6] Ross C A *et al* 2002 *Phys. Rev.* B **65** 144417
[7] Arrott A S and Templeton T L 1997 *Physica* B **233** 259
[8] Hubert A and Rave W 1998 *J. Magn. Magn. Mater.* **184** 67
[9] Aharoni A 1990 *J. Appl. Phys.* **68** 2892
[10] Guslienko K Y, Choe S B and Shin S C 2000 *Appl. Phys. Lett.* **76** 3609
[11] Porrati F and Huth M 2004 *Appl. Phys. Lett.* **85** 3157
[12] Shima H, Guslienko K Y, Novosad V, Otani Y, Fukamichi K, Kikuchi N, Kitakami O and Shimada Y 2002 *J. Appl. Phys.* **91** 6952
[13] de Graef M (ed) 2001 *Magnetic Imaging and its Applications to Materials* (San Diego, CA: Academic)
[14] Hopster H and Oepen H P (ed) 2005 *Magnetic Microscopy of Nanostructures* (Berlin: Springer)
[15] Dunin-Borkowski R E, McCartney M R and Smith D J 2004 *Encyclopaedia of Nanoscience and Nanotechnology* vol 3, ed H S Nalwa (Valencia, CA, USA: American Scientific Publishers) pp 41–100
[16] Carelli P and Foglietti V 1982 *J. Appl. Phys.* **53** 7592
[17] Bromwich T J, Kohn A, Petford-Long A K, Kasama T, Dunin-Borkowski R E, Newcomb S and Ross C A 2005 *J. Appl. Phys.* **98** 053909
[18] Bromwich T J 2005 *DPhil Thesis* University of Oxford
[19] Farhoud M, Ferrera J, Lochtefeld T J, Murphy T E, Schattenburg M L, Carter J M, Ross C A and Smith H I 1999 *J. Vac. Sci. Technol.* B **17** 3182
[20] Overwijk M H F, van den Heuval F C and Buelle-Lieuwma C W T 1993 *J. Vac. Sci. Technol.* B **11** 2021
[21] Saxton W O, Pitt T J and Horner M 1979 *Ultramicroscopy* **4** 343
[22] Frank J 1992 *Electron Tomography* (New York: Plenum)
[23] Press H, Flannery B P, Teukolsky S A and Vetterling W T 1996 *Numerical Recipes in Fortran: The Art of Scientific Computing* (New York: Cambridge University Press)
[24] Ross C A *et al* 2002 *J. Magn. Magn. Mater.* **249** 200
[25] Beleggia M and Zhu Y 2003 *Phil. Mag.* **83** 1045
[26] Ozkaya D, Langford R M, Chan W L and Petford-Long A K 2002 *J. Appl. Phys.* **91** 9937
[27] Ross C A, Chantrell R, Hwang M, Farhoud M, Savas T A, Hao Y, Smith H I, Ross F M, Redjdal M and Humphrey F B 2000 *Phys. Rev.* B **62** 14252